JACS
JOURNAL OF THE AMERICAN CHEMICAL SOCIETY
Article
pubs.acs.org/JACS

Si−H Activation in an Iridium Nitrido Complex—A Mechanistic and Theoretical Study

Daniel Sieh and Peter Burger*

Institut für Anorganische und Angewandte Chemie, Fachbereich Chemie, Universität Hamburg, Martin-Luther-King-Platz 6, 20146 Hamburg, Germany

Supporting Information

ABSTRACT: Si−H activation in triethyl- and triarylsilanes by a square-planar pyridine-diimine iridium complex with a terminal nitrido unit leads to the corresponding silyl amido complexes, which were unambiguously characterized by X-ray crystallography. Based on detailed combined kinetic and theoretical studies (DFT), direct addition of the Si−H bond to the iridium nitrido unit is proposed. The electronic propensities of the transition states for the Si−H activation were probed with a Hammett series of *para*-substituted triarylsilanes $HSi(C_6H_5)_2(4\text{-}C_6H_4\text{-}X)$. Based on the combination of experimental and theoretical studies, two independent pathways for this process are proposed, which point toward an ambiphilic propensity of the nitrido unit. Alternative pathways and the charge transfer in the transition states were also investigated. Furthermore, the barriers for the related H−H and C−H activation processes in dihydrogen and methane were analyzed.

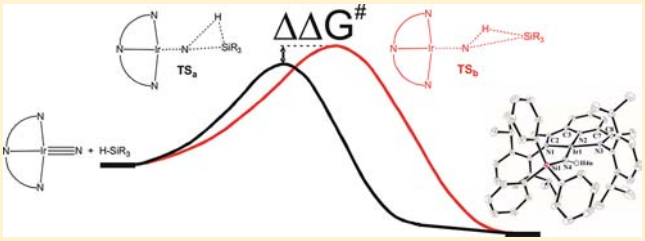

1. INTRODUCTION

Isolated middle to late transition metal complexes with a terminal metal nitrido unit, M≡N, still belong to an exclusive class of compounds. Recently published systems include d^4-configured iron, ruthenium, and iridium[1−7] as well as a square-planar d^6-configured iridium complex ($N_3Ir{\equiv}N$, **1**) discovered by our group.[8] Besides the most prominent reactivity pattern of this type of complexes to undergo dimerization to dinuclear μ-N_2-bridging complexes, $L_nM\text{-}N{\equiv}N\text{-}ML_n$,[5,7,9] the reactivity of these molecules is only little explored. Unfortunately, density functional theory (DFT) calculations on **1** and related systems suggest that dimerization to the μ-N_2-bridged complex is strongly energetically favorable (≫ −30 kcal/mol), revealing that this type of iridium nitrido system has little chance to become part of a Haber−Bosch catalytic process.[10] Due to the steric demand of the bulky aryl groups, complex **1** is apparently inert at ambient conditions.[10] At elevated temperatures, intramolecular ligand-based C−H activation processes were also observed for **1** and its related rhodium congener, leading to the formation of "tuck-in" complexes.[10] Similar observations were later reported for related (putative) ruthenium[11,12] and cobalt[13] nitrido transients. We recently showed that chloro protection of the vulnerable C−H bonds could suppress these undesired processes in an iridium system.[14]

Intermolecular activation steps in nitrido complexes were reported, for instance, by Smith et al. They observed a radical reaction of an iron nitrido complex with a suitable source of hydrogen atoms to yield ammonia.[15] Another example is a mass spectrometric study of C−H and N−H activation in the gas phase for a cationic iron nitrido complex by Schwarz et al.[16]

We have previously published the clean hydrogenation of the iridium nitrido compound **1** to the corresponding amido complex, $N_3Ir\text{-}NH_2$, under mild conditions (40 °C, <1 bar H_2). Based on DFT calculations, we suggested direct addition of H_2 to the electrophilic nitrogen atom of the nitrido unit without prior intervention of the iridium central atom.[8] Recently, Schneider et al. reported on H_2 addition to a Ru≡N unit in a ruthenium complex, which also gave an amido complex. The suggested mechanism for the Ru system differs from the proposed scheme for the iridium nitrido complex **1**, however, and involves a ligand-assisted H_2 activation step.[6] Herein, we present a detailed mechanistic and theoretical study of Si−H activation in hydrosilanes by the nitrido complex **1** to give the corresponding silyl amido systems, which provides further strong evidence for direct addition to the nitrido unit. We also focus on the origin of the barriers for these highly exothermic steps and include the related C−H bond activation process in the nitrido complex **1** and the corresponding protonated imido compound displaying an $Ir{=}NH^+$ imido unit.

2. RESULTS

The violet iridium nitrido complex **1** reacts at room temperature within minutes to hours with triethyl- and triarylsilanes to give the corresponding analytically pure brown and green silyl amido complexes **2** and **3-H** in 64 and 55% isolated yields, respectively (Scheme 1). When the reaction of excess triethylsilane with **1** was monitored by ^1H NMR spectroscopy, nearly quantitative conversion to the silyl

Received: December 6, 2012
Published: February 22, 2013

dx.doi.org/10.1021/ja311905h | J. Am. Chem. Soc. 2013, 135, 3971−3982

Scheme 1. Si−H Activation in the Nitrido Complex 1

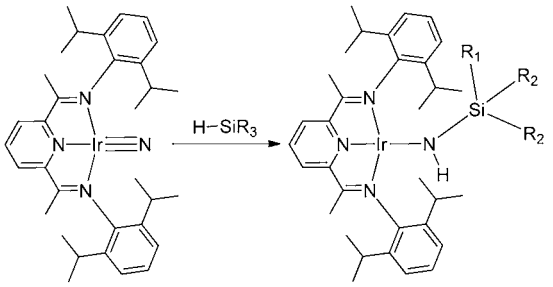

1

2: R_1=R_2=R_3=Et
3-OMe: R_1=4-C_6H_4-OMe; R_2=Ph
3-Me: R_1=4-C_6H_4-Me; R_2=Ph
3-tBu: R_1=4-C_6H_4-tBu; R_2=Ph
3-H: R_1=4-C_6H_4-H; R_2=Ph
3-Cl: R_1=4-C_6H_4-Cl; R_2=Ph
3-CF_3: R_1=4-C_6H_4-CF_3; R_2=Ph
4: R_1=R_2=Me, R_3=3-butenyl

amido complex **2** was noted, along with the formation of small traces (<2%) of a side product. Based on comparison of the NMR shifts, the side product was assigned as the previously isolated amido complex, N_3Ir-NH_2.[8] We anticipate that the latter is formed from reaction of adventitious water with the water-sensitive compound **2**. This view is supported by the reaction of isolated **2** with water to the amido complex, which argues against a stepwise reaction with initial H-radical abstraction from the silane (cf. below).

The products were fully characterized by 1-D and 2-D ^{1}H, ^{13}C-^{1}H, ^{15}N-^{1}H, and ^{29}Si-^{1}H NMR spectroscopy and elemental analyses. The time-averaged NMR spectra at room temperature were consistent with C_{2v} rather than C_s symmetry of complexes **2**, **3-R**, and **4**, which we previously rationalized for a related compound by a fast site exchange of the amido proton and the silyl groups.[14]

X-ray Crystal Structures of the Amido Products. This assignment was unambiguously confirmed by the results of X-ray crystal structure analyses for complexes **2**, **3-H**, **3-CF_3**, and **4**. Details of the data collection, solution, and refinement are provided in the Supporting Information. Since the molecular structures of **2**, **3-H**, **3-CF_3**, and **4** revealed essentially identical coordination geometries and geometrical parameters, we will highlight only the structural details of complex **3-H** (Figure 1). The constitution of the alkenyl silyl amido compound **4** will be briefly discussed within the mechanistic section.

The sum of angles around iridium (360.3°) observed in the crystal structure of complex **3-H** revealed an essentially planar metal center. As previously observed for this type of ligand framework, the N1−Ir1−N3 bond angle to the imine nitrogen atoms is significantly reduced from 180° to 156.52(7)° in **3-H**, such that its coordination geometry is best described as a pseudo-square-planar structure. The Ir−N4−Si1 angle is rather obtuse and displays a value of 148.61(11)°, which we recently rationalized on the basis of steric repulsion between the bulky triphenyl silyl and the N-aryl substituent.[14] This is also reflected in the asymmetric binding of the amido atom N4, which displays values of 109.64(7)° (N4−Ir1−N1) and 93.49(7)° (N4−Ir1−N3) for the bond angles to the imine atoms N1 and N3. The position of the amido proton H4n could be located in the difference Fourier map and was isotropically refined. This allowed us to estimate the sum of angles of the amido atom N4 at 359°, suggesting an sp^2-hybridized nitrogen center. The most

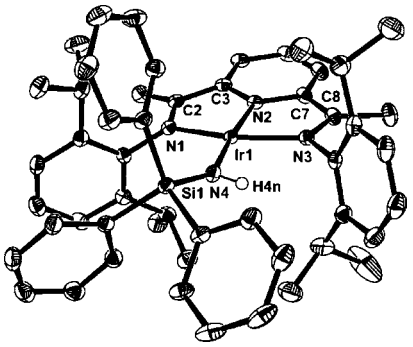

Figure 1. ORTEP plot at the 50% probability level for the X-ray crystal structure of the silyl amido complex **3-H** with selected bond length and angles. Ir1−N1, 2.046(2); Ir1−N2, 1.904(2); Ir1−N3, 2.023(2); Ir1−N4, 1.994(2); N4−Si1, 1.7202; N1−C2, 1.337(3); N3−C8, 1.331(3); C2−C3, 1.431(3); C7−C8, 1.433(3); N1−Ir1−N3, 156.52(7); N2−Ir1−N4, 171.50(8); N1−Ir1−N2, 78.34(7); N1−Ir1−N4, 109.64(7); N2−Ir1−N3, 78.80(7); N3−Ir1−N4, 93.49(7); Ir1−N4−Si1, 148.61(11); Si1−N4−H4n, 105(2); Ir1−N4−H4n, 105(2).

prominent feature in **3-H** is the Ir−N_{amido} bond length, which is stretched to 1.994(2) Å from the corresponding value of 1.646(9) Å for the Ir−$N_{nitrido}$ bond in the nitrido complex **1**,[8] suggesting a significantly lower bond order in the product.

Mechanistic Study of Hydrosilane Activation Kinetics. The mechanism of the hydrosilane activation in **1** was studied through a combined quantum-chemical and kinetic study. The kinetic analysis was carried out under pseudo-first-order conditions using excess silane. UV/vis kinetics was employed for all silanes using ∼10^{-4} mol/L solutions of the nitrido starting material **1**. The NMR kinetic analyses were performed for triethylsilane by integration of appropriate ^{1}H NMR integrals against ferrocene as internal standard and ensured comparable rates also for the higher concentration range of **1** employed in the NMR measurements (∼10^{-2} M). The following discussion is based on the more accurate UV/vis kinetic data.

The UV/vis kinetic traces for the reaction of **1** with silanes revealed clear isosbestic points and allowed us to rule out the presence of (long-lived) intermediates with sizable concentrations (Figure 2, top).

Logarithmic plots of $\ln([\mathbf{1}]/[\mathbf{1}]_{t=0})$ vs time for the decay of the nitrido starting material **1** revealed excellent linear relationships (R^2 = 0.999) over 5 half-lives (Figure 2, bottom). This clearly suggested a first-order dependence on [**1**] for the silane addition to **1**. This view was supported by comparison with the rates of formation for the silane products **2** and **3**: Essentially identical rate constants for the decay of **1** and formation of their corresponding silyl amide products **2** and **3** were observed.

Plots of the observed rate constant, k_{obs}, for the decay of **1** vs the silane concentration revealed a linear dependence consistent with an overall second-order rate law. This is shown in exemplary fashion for the reaction of **1** with $HSiEt_3$, from which a second-order reaction rate constant k_{sec} = 2.00(15) L/mol·s at 298 K was derived (Figure 3, top).

Further mechanistic evidence was obtained from an Eyring plot[17] of the temperature-dependent second-order rate constants in the range of 283−323 K. For the reaction of **1** with triethylsilane (**1** + $HSiEt_3$ → **2**), a small value of $H^{\#}$ = 10.3(2) kcal/mol for the enthalpy of activation and a strongly

dx.doi.org/10.1021/ja311905h | J. Am. Chem. Soc. 2013, 135, 3971−3982

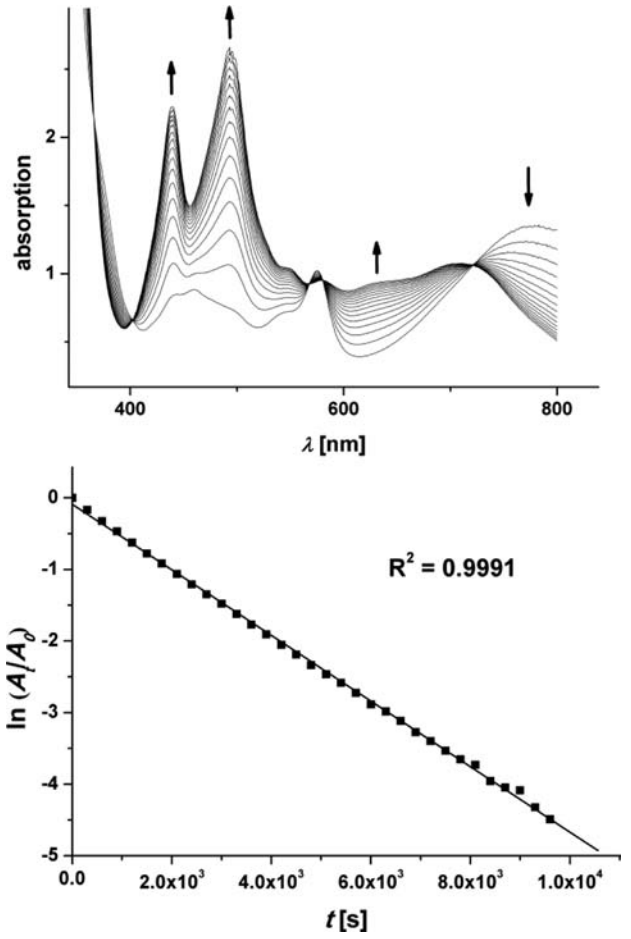

Figure 2. UV/vis monitoring of the transformation **1** + $HSiEt_3$ → **2** (top) and first-order decay (bottom).

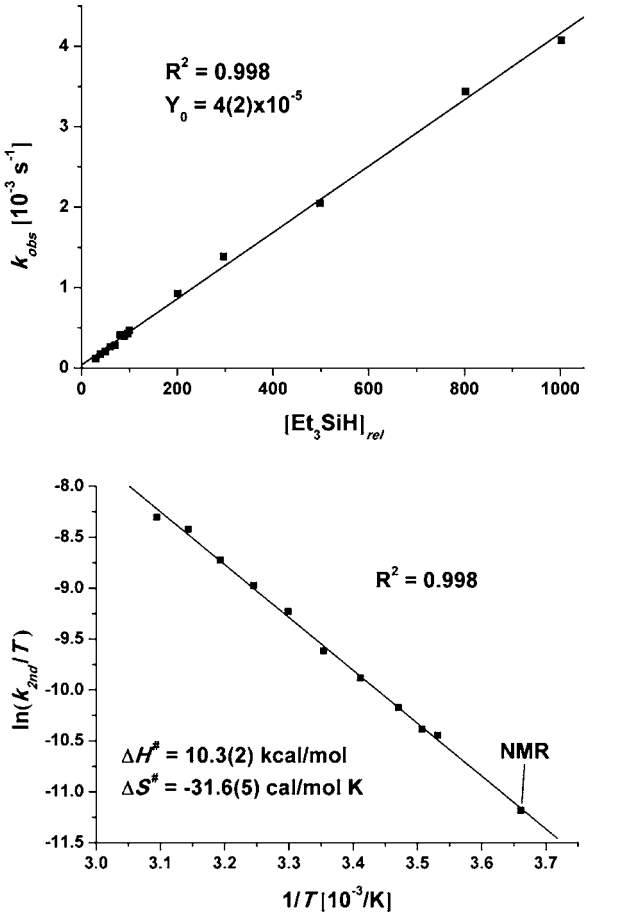

Figure 3. Second-order dependence (top) and Eyring plot for the transformation **1** + $HSiEt_3$ → **2** (bottom).

negative activation entropy of $\Delta S^{\#} = -31.6(5)$ cal/mol·K were derived (Figure 3, bottom).

Finally, the kinetic isotope effect (KIE) was probed in the reaction of **1** with the mono-deuterated isotopologue, deuteriotriethylsilane ($DSiEt_3$), at 298 K. The observed KIE, k_H/k_D = 1.8, is sizable considering the estimated maximum classic isotope effect of 4 (based on ν(SiH) = 2100 cm^{-1} for $HSiEt_3$). This suggested participation of the Si–H bond-breaking process in the transition state.

Dependence on Solvent Polarity. Further mechanistic evidence was deduced from the influence of the solvent polarity on the kinetics for the Si–H activation process according to Scheme 1. We therefore determined the second-order rate constants for the reaction of **1** with triethylsilane in toluene, ether, and THF, which display dielectric constants of 2.4, 4.3, and 7.6, respectively, at 298 K. The results are presented in Figure 4.

Faster rates are observed in solvents of lower polarity: the second-order rate constant in toluene is approximately twice as fast in THF.

Radical Clock and Crossover Experiments. In order to probe for radical steps in the Si–H activation process, we investigated the reaction of **1** with the 3-butenyl-substituted hydrosilane[18] (cf. Scheme 1). Hydrogen abstraction from the silane by the nitrido complex would lead to the imido complex **1-H** and the corresponding silyl radical **a** (Scheme 2).

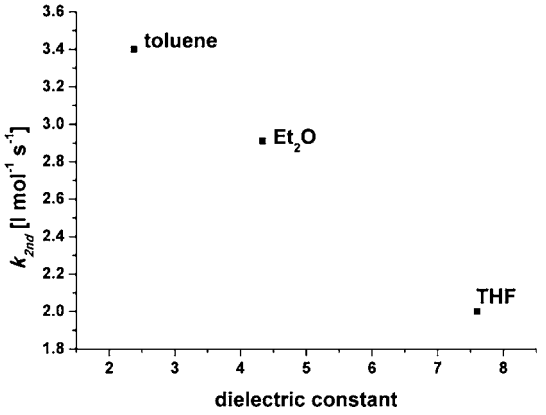

Figure 4. Second-order rate constants for the transformation **1** + $HSiEt_3$ → **2** in solvents of different polarity.

The silyl radical **a** could either collapse with **1-H** to give the observed product **4** or undergo *intramolecular* ring closure prior to the recombination with **1-H**. The rate for the ring closure is high and yields the five-membered ring shown here, with a

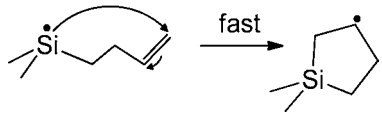

carbon-centered radical. Should the silyl radical **a** be formed in the course of the reaction, then the amido complex **4a** would

dx.doi.org/10.1021/ja311905h | J. Am. Chem. Soc. 2013, 135, 3971–3982

Scheme 2. Possible Products of a Radical Pathway

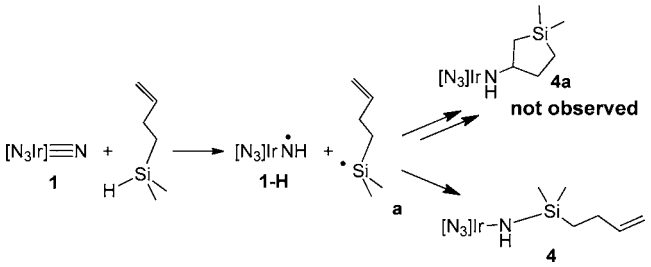

therefore be a likely product (Scheme 2, top path). Within NMR detection limits, we were not able to observe the formation of **4a** but rather isolated exclusively the open-chain product **4**. The latter was unambiguously characterized by ^{1}H and ^{13}C NMR spectroscopy and X-ray crystallography (Figure 5).

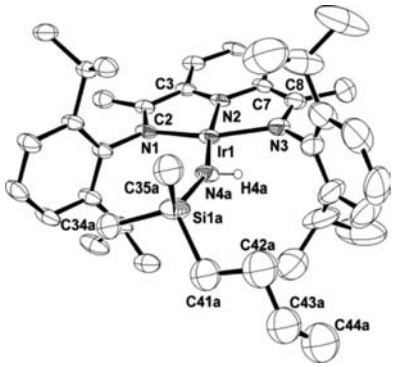

Figure 5. X-ray crystal structure of complex **4** (ORTEP plot at the 30% probability level). The butenyl group is disordered over two positions; only one of these positions is shown.

This result does not completely rule out radical pathways for the Si–H activation step. The rate for recombination of the radical pair **1-H** and compound **a** would have to be faster, though, than the cyclization step of the Si-centered radical with an estimated half-life of $<10^{-7}$ s. The latter value is based on experimental cyclization rate constants of comparable silyl radicals, which are in the range of 10^{7}–10^{9} s^{-1}.[19,20]

In another set of experiments, we studied the reaction of **1** with a mixture of trimethylsilane and $DSiEt_3$ according to Scheme 3.

We could clearly establish the direct adducts **2-D** and **5** as major components of the product mixture (cf. Supporting Information). The NMR spectroscopic analysis was nevertheless not fully conclusive, since we cannot securely rule out

Scheme 3. Double-Label Crossover Experiments

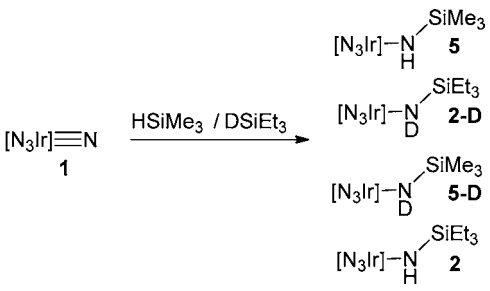

the formation of the additional crossover products **2** and **5-D**, which could be formed in radical-type hydrogen/deuterium abstraction processes. The outcome of the reaction with the radical clock silane substrate and the latter results were taken as a hint, however, that radical pathways are less likely for the hydrosilane activation in the nitrido complex **1**.

Hammett Substituent Study. In order to shed further light on the mechanism of the silane activation process, we investigated the kinetics for a series of triarylsilanes of the type, $HSiPh_2(4\text{-}C_6H_4\text{-}R_1)$. The substituents R_1 in the *para*-position of the phenyl ring were chosen to span a wide range of Hammett σ_{para} parameters, i.e., R_1 = OMe (σ_{para} = −0.27) to R_1 = CF_3 (σ_{para} = 0.54).[21,22] The Hammett plot[23] for these silanes is shown in Figure 6.

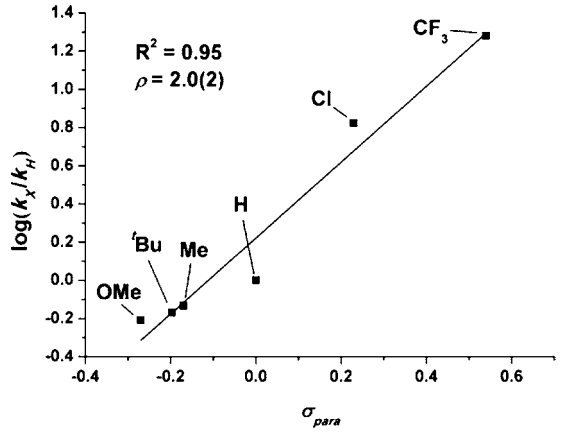

Figure 6. Hammett plot for the reaction of **1** + $HSiPh_2(4\text{-}C_6H_4\text{-}R_1)$ → **3-X**.

Before we turn to the analysis of the Hammett plot, it shall be briefly mentioned that we had also included the dimethylamino-substituted silane, $HSiPh_2(4\text{-}C_6H_4\text{-}NMe_2)$, in this study. Contrary to the other silanes, however, which gave (i) pure silyl amido products **3** and (ii) highly reproducible kinetics, the reaction of this unique silane with **1** led to highly erratic kinetic results. We have therefore decided to exclude this silane in the Hammett plot.

Inspection of the Hammett plot presented in Figure 6 reveals a good linear relationship (R^2 = 0.95) with a positive value for the reaction constant ρ_{exp} = 2.0. This points toward to a substantial buildup of negative charge in the transition state; hence, hydrosilanes with more electron-withdrawing groups react faster!

This clearly contradicted our working hypothesis that the Si–H activation proceeds exclusively by nucleophilic attack of the Si–H bond at the electrophilic iridium nitrido unit. Finally, it shall be briefly mentioned that the CF_3-substituted silane, $HSiPh_2(4\text{-}C_6H_4\text{-}CF_3)$, was initially not included in our study, since it is not commercially available. The notable curvature of the Hammett plot observed for the smaller range of Hammett parameters without this silane persuaded us to include the trifluoromethyl-substituted silane in our investigations, however. The kinetic results for the latter silane unambiguously established a *linear* Hammett plot, i.e., fully consistent with an uniform reaction pathway for all silanes.

Our initial anticipation of a *curved* Hammett plot observed for the smaller number of silanes was therefore *erroneous*. Its consideration proved to be nevertheless highly instrumental,

dx.doi.org/10.1021/ja311905h | J. Am. Chem. Soc. 2013, 135, 3971–3982

since it prompted us to look thoroughly into (alternative) reaction mechanisms for the Si−H activation step in the DFT calculations.

Theoretical Study. First, we looked into the thermodynamics of the silane activation processes. In analogy to our previous results for the addition of dihydrogen to **1**,[8] our DFT calculations revealed strongly energetically favorable situations for the formation of the silyl amido complexes **2** and **3-X** according to Scheme 1 for all silanes with reaction energies of ∼−40 kcal/mol (cf. Supporting Information). Next, we initiated a transition-state search for the Si−H activation in SiH_4 for the small model complex, **1-model**, in which the aryl

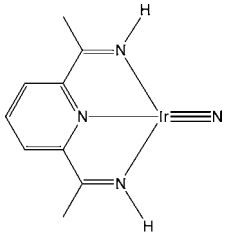

1-model

substituents of the imine groups were replaced by hydrogen atoms. We located two different transition states within 7 kcal/mol for the silane activation in the model complex **1-model**. Intrinsic reaction coordinate (IRC) calculations for these two transition states confirmed that both connected the starting materials, i.e., SiH_4 and the complex **1-model**, with the corresponding silyl amido product (Ir−N(H)Si(H_3)) related to **2** and **3**.[24] Based on the calculations for the model systems, we performed TS searches for the Si−H activation process in triphenylsilane for the full nitrido complex, i.e., **1** + $HSiPh_3$ → **3-H**. Gratifyingly, we were able to locate also two analogous transition states, denoted as $\mathbf{TS_a}$ and $\mathbf{TS_b}$, which are presented in Figure 7.

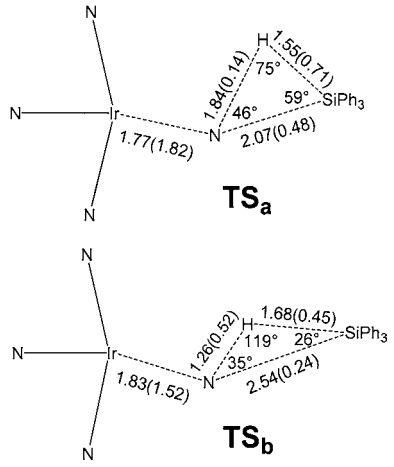

Figure 7. DFT-optimized geometries of the transition states $\mathbf{TS_a}$ and $\mathbf{TS_b}$ with selected bond distances [Å] and angles [°] for **1** + $HSiPh_3$ → **3-H** and with Mayer bond orders in parentheses.

The corresponding IRC calculations for both $\mathbf{TS_a}$ and $\mathbf{TS_b}$ allowed us to unambiguously confirm that there are indeed two independent reaction pathways. The energy difference $\Delta\Delta E_a = \Delta E_a(\mathbf{TS_b}) - \Delta E_a(\mathbf{TS_a})$ of the computed barriers amounts to 0.8 kcal/mol ($\Delta E_a(\mathbf{TS_a})$ = 19.2, $\Delta E_a(\mathbf{TS_b})$ = 20 kcal/mol) and reveals a small preference for $\mathbf{TS_a}$, but nevertheless provides support that *both* competing pathways may be operative (cf. below). These can be differentiated through the progress of the N−H and N−Si bond formation and Si−H cleavage processes and display different stages of their corresponding transition states. The description of $\mathbf{TS_a}$ and $\mathbf{TS_b}$ as early and late transition states would be overly simplistic. Some support for such a view might be nevertheless taken from inspection of Figure 7 in view of the bond cleavage process and the necessary adaptation of the $Ir-N_{nitrido,amido}$ bond on going from **1** + $HSiPh_3$ → **3-H**, i.e., starting with a bond order close to 3 in the nitrido complex **1** and ending up with a formal single bond in the amido compound **2** (exp: **1**, $Ir-N_{nitrido}$ = 1.646(9) Å; **3-H**, $Ir-N_{amido}$ = 1.994(2) Å).[8]

The corresponding coordinates of the minimum energy paths (MEPs) for $\mathbf{TS_a}$ and $\mathbf{TS_b}$ were employed for the calculation of the Mayer bond orders along the reaction path (Figure 8).

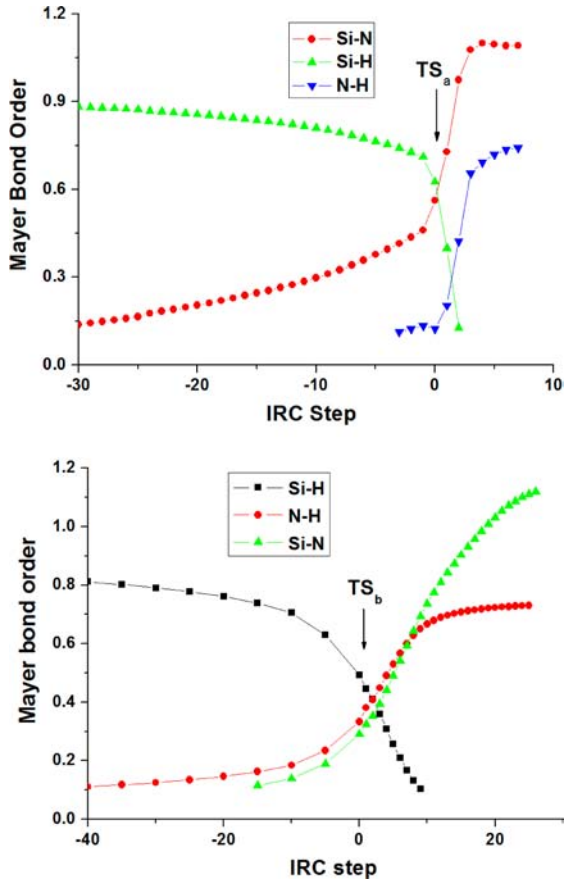

Figure 8. Mayer bond orders along the MEPs of the corresponding transition states $\mathbf{TS_a}$ (top) and $\mathbf{TS_b}$ (bottom) for the reaction **1** + $HSiPh_3$ → **3-H**.

Related transition states $\mathbf{TS_a}$ and $\mathbf{TS_b}$ were located for the Si−H activation in all silanes presented in Scheme 1. For the quantum-chemically derived Hammett plot, we also included the nitro- and amino-substituted silane derivatives, HSi-(C_6H_5)$_2$(4-C_6H_4-(NO_2 or NH_2)), to extend the available range of Hammett σ_{para} constants from −0.66 to 0.78 with these excellent electron-withdrawing and -releasing groups. The Hammett plot shown in Figure 9 is based on the data for $\mathbf{TS_a}$ and reveals an excellent linear relationship (R^2 = 0.989). The

dx.doi.org/10.1021/ja311905h | J. Am. Chem. Soc. 2013, 135, 3971−3982

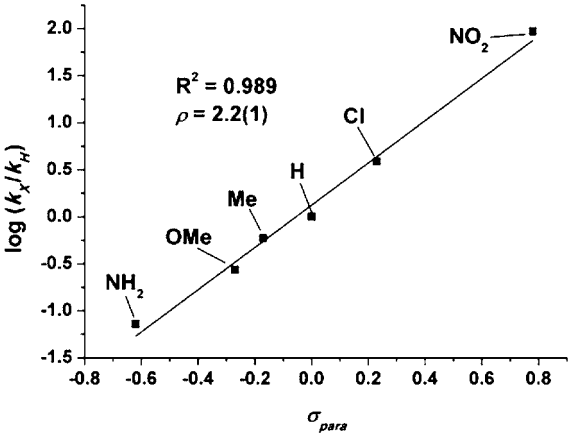

Figure 9. Hammett plot for the reaction of **1** + $HSiPh_2(4\text{-}C_6H_4\text{-}R_1)$ → **3-X** for TS_a based on DFT calculations.

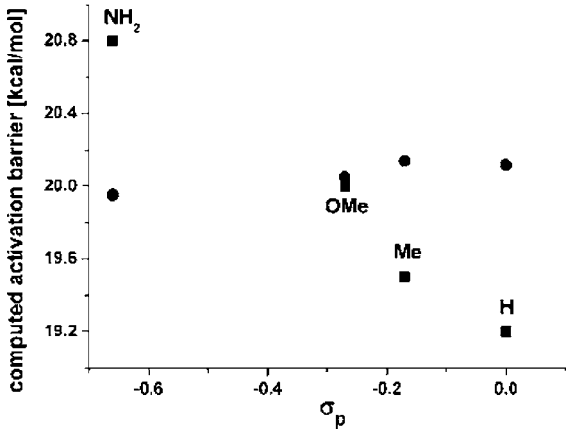

Figure 10. Calculated activation barriers for **1** + $HSiPh_2(4\text{-}C_6H_4\text{-}X)$ → **3-X** for TS_a (■) and TS_b (●).

good agreement of the experimental and DFT-derived reaction constants, ρ_{exp} = 2.0 and ρ_{calc} = 2.2, is particularly noteworthy.

For TS_b, on the other hand, we did not observe a similar correlation between the Hammett parameters and the calculated barriers (Figure 10).

Further mechanistic insight was obtained from Natural Bond Orbitals (NBO)[25−27] and Absolutely Localized Molecular Orbital Energy Decomposition and Charge Transfer Analyses (ALMO-EDA/ALMO-CTA).[28,29]

NBO Analysis. In TS_a, one of the Si−C_{aryl} bonds of the silane is essentially located in the plane of the terdentate ligand framework. The corresponding bond distance is elongated by 0.05 Å compared to the values of the related two other Si−C bonds, which are essentially unchanged from the bond lengths in the free silane. This observation could be explained by second-order perturbation NBO analysis. The latter revealed donation from the lone pair centered on the sp-hybridized nitrido nitrogen atom to the σ^*-acceptor orbital of the in-plane Si−C_{aryl} bond (Figure 11), leading to a significant stabilization by −29.9 kcal/mol.

ALMO-CTA/EDA. The ALMO-CTA and ALMO-EDA methods described by Head-Gordon et al. allow us to calculate the amount of charge transfer and interaction energies between (molecular) fragments.[28,29] Periana et al. used this technique to classify the nature of C−H activation processes according to their electro-, nucleo-, or ambiphilicity based on the amount of

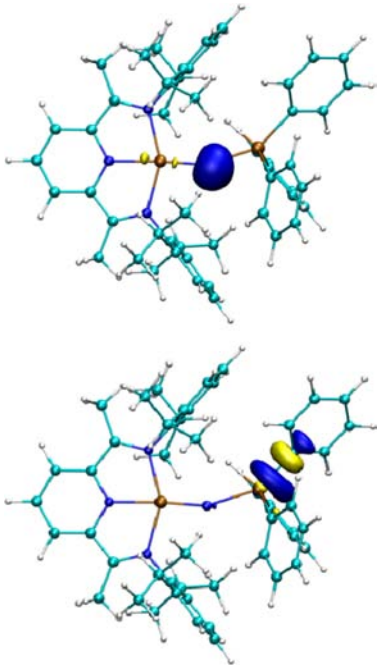

Figure 11. Orbitals involved in second-order perturbation in TS_a for **1** + $HSiPh_3$ → **3-H** (top, nitrido lone pair; bottom, in-plane σ^*-Si−C_{aryl} orbital).

charge transfer between the substrate and the metal fragment in the transition state.[30,31]

We applied ALMO-EDA/CTA for the investigation of the Si−H silane activation steps in TS_a and TS_b and also for activation of the dihydrogen and methane molecules by the nitrido model complex **1-model**. The results of these calculations are summarized in graphical form in Figures 12 and 13, where the involved complementary occupied virtual pairs (COVPs) are presented.

There is a strong disparity between the ALMO results for TS_a and TS_b (Figure 12). According to the EDA, the interaction energies for the Si−H activation process in TS_a are significantly smaller than in TS_b, i.e., only about one-half of the values for donation from the lone pair of the nitrido unit and from the Si−H bond of the silane in TS_b. This is also reflected in the results for the CTA between the two fragments in $TS_{a,b}$. However, in this case charge transfer from the nitrido lone pair to the silane is essentially identical (TS_a, 32 me^-; TS_b, 33 me^-). Charge transfer from the silane in TS_b to the nitrido complex, on the other hand, amounts to more than 1 e^- (1070 me^-) and nearly doubles the value derived for TS_a (584 me^-).

A comparison of the ALMO-EDA and ALMO-CTA results for $TS_{a,b}$ of the Si−H bond cleavage in silanes with the data for H−H and C−H activation in dihydrogen and methane reveals that TS_b closely resembles the transition states for the latter two processes (Figure 13). This is based on the values from both ALMO-EDA and ALMO-CTA, which clearly evidence that the donation from dihydrogen and methane to the nitrido unit strongly dominates over the reverse interaction.

The barriers for the activation in dihydrogen and in methane by the model complex amount to 23 and 35 kcal/mol, respectively. With the aid of the orbital occupancy-perturbed bond order method[32] implemented in the AOMIX program[33] or NBO's natural steric analysis,[25−27] they can be traced to four-electron, two-orbital repulsive interactions between the filled σ-orbitals (H−H and C−H) and the lone pair of the

dx.doi.org/10.1021/ja311905h | J. Am. Chem. Soc. 2013, 135, 3971−3982

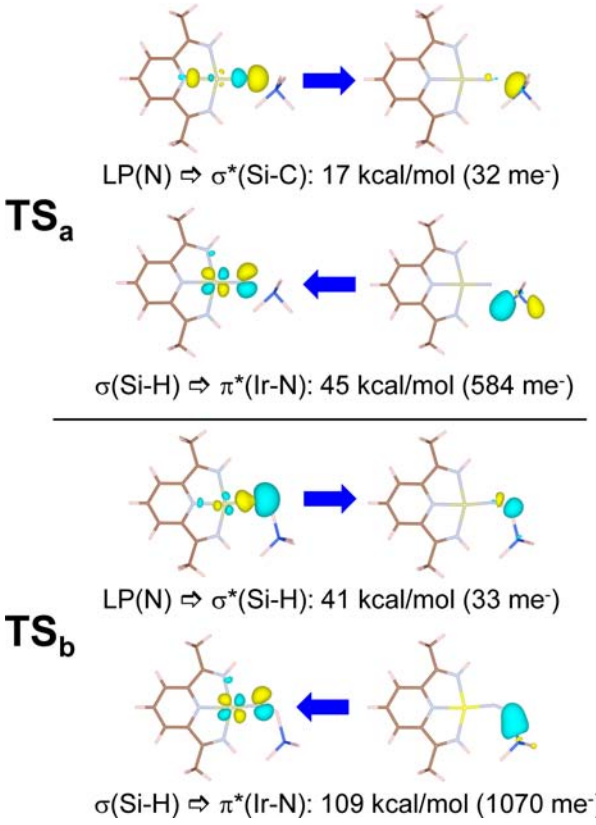

Figure 12. Complementary occupied virtual pairs with major contributions to the charge transfer and energy decomposition analyses for the silane activation in SiH_4 by the model complex **1-model** (top, TS_a; bottom, TS_b).

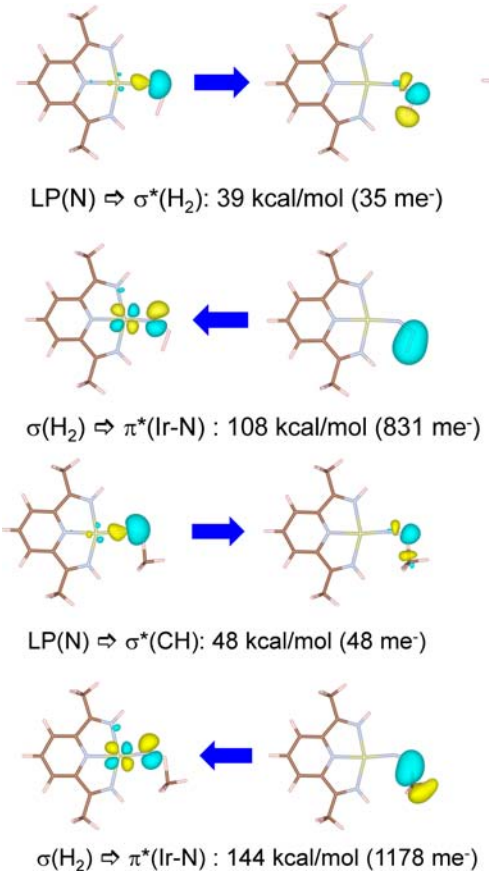

Figure 13. Complementary occupied virtual pairs with major contributions to the charge transfer and energy decomposition analyses for the activation in H_2 (top) and CH_4 (bottom) (upper traces, donation from the nitrido model complex to the substrates; lower traces, back-donation from the substrates).

nitrido nitrogen atom in the transition states. This is shown in Figures 14 and 15.

3. DISCUSSION

Based on DFT calculations and analysis of the Fukui function for the hydrogenation of complex **1** to the corresponding amido compound ($N_3Ir{\equiv}N + H_2 \rightarrow N_3Ir\text{-}NH_2$), we previously proposed direct addition of dihydrogen to an *electrophilic* nitrido unit. There is also full support for direct Si−H bond addition of the hydrosilanes to the nitrido nitrogen atom from the experimental and theoretical studies.

First, the clean isosbestic points in the UV/vis kinetic trace rule out the formation of long-lived intermediates (Figure 2). This is also supported by ^{1}H NMR monitoring of the reaction of triethylsilane with **1**, which showed only the resonance of the starting materials and products. Second, the established second-order rate law for the addition of the silanes and the strongly negative entropy of activation ($\Delta S^{\#} = -32$ cal/mol·K, Figure 3) for the triethylsilane substrate also provide evidence for the proposed direct addition mechanism.

On the other hand, analysis of the Hammett plot for the series of *para*-substituted triarylsilanes (Scheme 2 and Figure 6) argued strongly against our concept of an (exclusive) electrophilic nitrido unit in the transition state. While for addition to an *electrophilic* nitrido unit faster rates were expected for substituted silanes with donor substituents, e.g., methyl or OMe groups, we had to witness that electron-withdrawing groups led to increased second-order rate constants. Since the positive reaction constant (ρ_{exp} = 2.0) derived from the Hammett plot and the experimental activation enthalpies (cf. Experimental Section) are reproduced well in the DFT calculations for TS_a (ρ_{calc} = 2.2, cf. Figures 6 and 9), we are confident that the corresponding calculated transition states are good models of the real electronic situation. Further

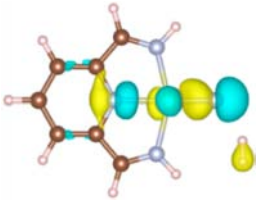

Figure 14. Four-electron, two-orbital repulsive interaction in the transition state for the H−H activation in dihydrogen (AOMIX).

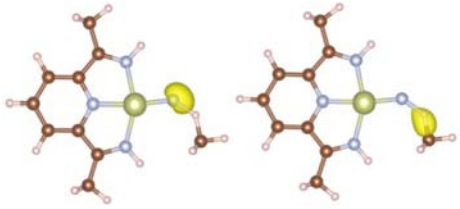

Figure 15. PNLMOs involved in four-electron, two-orbital repulsive interaction in the transition state for the C−H activation in methane (NBO).

dx.doi.org/10.1021/ja311905h | J. Am. Chem. Soc. 2013, 135, 3971−3982

support for this view was provided from DFT calculations in solution, in which a dielectric continuum model (COSMO) was applied. In agreement with the experimental findings for the addition of triethylsilane to the nitrido complex **1** (Figure 4), smaller reaction barriers were calculated for solvents of lower polarity. This is traced to the large change of the dipole moments going from the highly polar starting material, which amounts to ∼5 D in **1** according to DFT calculations and substantially smaller values in the transition states. The latter display strongly reduced dipole moments of only 2 D.

An explanation for faster reaction rates for silanes with electron-withdrawing substituents was provided by the analysis of the geometry and electronic structure of $\mathbf{TS_a}$. The slight elongation of one of the Si−C_{aryl} bonds by 0.05 Å and the results of the NBO second-order perturbation analysis revealed donation from the (sp-hybridized) nitrido lone pair to the σ^*-orbital of this unique Si−C_{aryl} bond, leading to a stabilization by −29.9 kcal/mol (Figure 11). This is further supported by the rather short $N_{nitrido}$−Si distances in the range of 2.0−2.1 Å in $\mathbf{TS_a}$ (Figure 7 top for **3-H**), which suggests strong N−Si interactions in the transition states and is also reflected in the calculated Mayer bond orders of ∼0.6 in $\mathbf{TS_a}$. It deserves a special mention that the value for the Mayer bond order of the Si−H bond is reduced by 0.3 unit in the $\mathbf{TS_a}$ (Figure 7 top), which is consistent with the observed deuterium KIE, k_H/k_D = 1.8 for the Si−H activation in triethylsilane, i.e., some degree of Si−H/D bond cleavage. Based on these results and monitoring of the IRC trace leading to $\mathbf{TS_a}$ shown in Figure 8, the Si−H activation process is best described as initial attack of a *nucleophilic* nitrido nitrogen atom at the Si center of the silane.

Further insights were obtained from energy decomposition and charge transfer analyses according to Head-Gordon's ALMO-EDA/CTA methods, which shed a slightly modified light on this issue, however. For the model SiH_4 substrate, an electron transfer of 32 me^- and an interaction energy of 17 kcal/mol were calculated for the donation from the model nitrido complex **1-model** to the silane. The corresponding COVPs identified the nitrido lone pair and the unoccupied σ^*-bond orbital of a distant Si−H bond as the major components (Figure 12). However, this contribution is strongly overruled by donation from a filled orbital of an adjacent Si−H bond, which displays a charge transfer from the silane of 534 me^- and an interaction energy of 45 kcal/mol. The analysis of the COVPs clearly revealed that the Ir−$N_{nitrido}$ π^*-orbital of the nitrido complex is the dominant charge acceptor from the silane (Figure 12). While we anticipated this type of donor/acceptor couple on the basis of our previous DFT analysis for the activation in dihydrogen, based on our Hammett analysis we were nevertheless somewhat surprised that donation from the silane to the metal fragment was dominating to such an extent over the reverse charge flow from the nitrido unit to the silane in $\mathbf{TS_a}$.

For comparison, complementary analyses were performed for the Si−H activation in SiH_4 according to $\mathbf{TS_b}$ and the transition states for H−H and C−H bond cleavage in dihydrogen and methane. First, it is noteworthy that the calculated barriers of 23 (H_2) and 35 kcal/mol (CH_4) for the latter substrates are significantly larger than for the hydrosilanes (calc barriers: 17−20 kcal/mol), while all reactions are strongly thermodynamically favorable (H_2, −54 kcal/mol; CH_4, −30 kcal/mol; R_3SiH, ∼ −40 kcal/mol). It is noteworthy that the abstraction of an H radical according to $[Ir]{\equiv}N + RH \rightarrow [Ir]{=}NH + R^{\bullet}$ is estimated to be extremely energetically uphill for hydrogen and methane and less unfavorable for SiH_4 (R = H, +45 kcal/mol; R = Me, +44 kcal/mol; R = Si, +26 kcal/mol), which is anticipated on the basis of the lower Si−H bond dissociation enthalpy (90 (Si−H) vs ∼105 kcal/mol (H−H, H_3C−H)). The transition-state geometry $\mathbf{TS_b}$ for the hydrosilane and the transition states for the dihydrogen and methane substrates show a strongly related pattern (Figure 7 bottom and Supporting Information), i.e., very short N···H distances to the hydrogen atom of the activated Si−H, H−H, and C−H bonds. The N−Si,H,C distances of the nitrido atom to the other bonding partner, on the other hand, are quite large (N−Si, 2.54 Å; N−H, 1.78 Å; N−C, 2.24 Å), questioning the bonding situation between these partners in the transition states. This point will be addressed later in the context of potential rebound/radical mechanisms. Furthermore, in contrast to $\mathbf{TS_a}$, substantial elongation of the activated Si−H bond is observed in $\mathbf{TS_b}$ (Figure 7: 1.55 vs 1.68 Å), which is also noted for the H−H/C−H bonds in the H_2 and CH_4 substrates (H−H, 1.12 Å; H_3C−H, 1.61 Å) in comparison with their experimental values of 0.74 and 1.09 Å in free dihydrogen[34] and methane.[35] This elongation of the activated bonds suggested substantial charge transfer to an *electrophilic* nitrido nitrogen atom originating from the filled σ-orbital of the substrate's Si−H, H−H, and C−H bonds or, vice versa, electron donation from a *nucleophilic* nitrido center to the corresponding σ^*-orbitals. Alternatively, a combination of both factors could be operative, leading to a situation in which the nitrido atom would be best described as *ambiphilic*. This type of propensity of a nitrido ligand was previously discussed by the groups of Berry[36] and Sauer.[37]

The results of the ALMO-EDA/CTA calculations shown in Figures 12 (bottom) and 13 clearly reveal that both factors are contributing, i.e., that electron donation from the substrates to the nitrido unit and vice versa plays a role. However, ALMO-EDA and in particular ALMO-CTA unambiguously evidence that donation from the substrates to the nitrido unit is dominating. This can be seen from the interaction energies which are 2.5−3-fold larger for the donation from the SiH_4, H_2, and CH_4 substrates to the metal fragment in the transition state compared to the reverse situation (SiH_4, 49 vs 109 kcal/mol; H_2, 39 vs 108 kcal/mol; CH_4, 48 vs 144 kcal/mol). This is even more pronounced for the values calculated for charge transfer, which are in the range of 1 e^- (SiH_4, 1070 me^-; H_2, 831 me^-; CH_4, 1178 me^-), while only 33−48 me^- are transferred back from the nitrido unit to the substrates. Therefore, it is conceived that the nitrido nitrogen atom reacts predominantly as an *electrophile* in $\mathbf{TS_b}$ and in the transitions states for the activation of H_2 and methane.

Two further points remain to be addressed: (i) Does $\mathbf{TS_b}$ correspond to a radical/rebound mechanism? (ii) What is the origin of the calculated substantial barriers for the activation in H_2 and methane of 23 and 35 kcal/mol? The latter are significantly larger than for the silane substrates and would not be anticipated on the basis of the Bell−Evans−Polanyi principle for these strongly exothermic reactions with calculated reaction energies of ∼ −30 to −50 kcal/mol.

Item (i) was addressed by both theoretical and experimental methods. The potential radical character of the silane addition was probed (a) with a radical clock substrate (Scheme 2) and (b) in crossover experiments. In the reaction of the radical clock substrate dimethyl-3-butenylsilane (Me_2(3-butenyl)SiH) with **1**, ^1H and ^{13}C NMR analysis of the silyl amido product revealed exclusive formation of the open-chain product **4**,

dx.doi.org/10.1021/ja311905h | J. Am. Chem. Soc. 2013, 135, 3971−3982

which was confirmed by X-ray crystal structure analysis (Figure 5). This result does not unambiguously rule out a radical pathway. Based on the known cyclization rate constant for a related free silyl radical compound, the absence of the cyclized product **4a** would, however, require a very fast recombination rate constant for the open-chain silyl and imido radicals of at least 10^7 s^{-1}. Further evidence for a *nonradical* pathway was sought from the crossover experiment employing **1** and a mixture of $HSiMe_3$ and $DSiEt_3$ (Scheme 3). Although the latter experiment was unfortunately not fully conclusive, we could show that the product is almost exclusively the corresponding direct addition product, in which no crossover had occurred. Combining the outcomes of these two experiments, we anticipate that Si−H addition in the investigated silanes proceeds by nonradical pathways. Obviously, these results do not distinguish between the two pathways with the corresponding $\mathbf{TS_a}$ or $\mathbf{TS_b}$.

Further support for nonradical pathways stems from the analysis of the corresponding MEP for $\mathbf{TS_b}$. As anticipated from the aforementioned significant Si−H bond elongation in the transition state, the Mayer bond order for the Si−H bond drops continuously from 0.9 to 0.5 in $\mathbf{TS_b}$ (Figure 8 bottom). However, at the same time, both the Ir−N−H *and* Si−N Mayer bond orders increase to reach values of ∼0.5 in the transition state. Together with the N−H−Si angle of 119° in $\mathbf{TS_b}$, we take this as a hint for nonradical pathways. In rebound mechanisms by contrast, e.g., in the activation of methane by metal oxo systems, the bond angle at the abstracted hydrogen atom (M═O···H···CH_3) is usually nearly linear.[38−41] Furthermore, DFT calculations of the S = 0 and S = 1 states for $\mathbf{TS_b}$ revealed a clear preference of 31 kcal/mol for the singlet state, which also argues against the occurrence of "free radicals".

Finally, we will address the origin of the calculated substantial barriers for the analogous H−H and C−H activation processes in dihydrogen and methane (23 and 35 kcal/mol). Gorelsky's "orbital occupancy-perturbed bond orders" method was utilized to identify a unique occupied molecular orbital (MO)[32] which contributes strongly to the activation barrier. Inspection of this MO reveals a four-electron, two-orbital repulsive interaction between the σ-orbital of H_2 and the lone pair of the sp-hybridized nitrido nitrogen atom (Figure 14). For both the hydrogen and methane substrates, an analogous destabilizing situation was established from an NBO steric analysis, which revealed a steric repulsion of ∼60 kcal/mol (Figure 15 and Supporting Information). As discussed above in the NBO analysis, this type of repulsion is diminished in the silane substrates by additional interaction of the nitrido lone pair with a moderately low-lying Si−C σ*-acceptor orbital (Figure 11). Note that for the methane analogue a corresponding σ*-C−H orbital cannot play a comparable role due to its higher energetic position and contraction. The transition states for both H_2 and methane substrates therefore resemble the alternative $\mathbf{TS_b}$ of the silanes and can be interpreted as *electrophilic attack* of the nitrido moiety.

From this perspective, it becomes clear that protonation of the nitrido's lone pair should lower the energetic barrier for the activation processes in H_2 and methane. This is indeed the case, as we previously demonstrated experimentally by a significant enhancement for addition of H_2 to **1** in the presence of an acid.[8]

4. CONCLUSION

Our complementary experimental and theoretical studies clearly show that the unique terminal nitrido complex **1** displays both electrophilic and nucleophilic properties. Depending on the substrate employed in the bond activation processes, either of them can dominate the reaction paths. The observed barriers were traced to four-electron, two-orbital repulsive interactions, involve the lone pair of the nitrido moiety, and can be lowered through its protonation. A related increase of reactivity is expected for the oxidized nitrido complex $\mathbf{1}^+$. This research is currently being pursued in our laboratory and excavates exciting C−C activation processes, which will be reported in due course.

5. EXPERIMENTAL SECTION

General. All manipulations were carried out using standard Schlenk, glovebox, and high-vacuum manifold techniques under an atmosphere of high-purity nitrogen. Pentane, tetrahydrofuran (THF), toluene, diethyl ether (Et_2O), and hexamethyldisiloxane (HMDSO) were distilled over sodium benzophenone ketyl. ^1H, ^{13}C, ^{15}N, and ^{29}Si NMR spectra were recorded on Bruker Avance 400 and Varian Gemini 2000 BB NMR spectrometers. The ^1H and ^{13}C NMR spectra are referenced to the residual resonances of the solvent. The ^{15}N NMR shifts are referenced to NH_3 ($\delta(NH_3)_{(l)}$ = −380 ppm vs $MeNO_{2(l)}$). The ^{29}Si NMR shifts are referenced to Me_4Si. The assignments of the ^{13}C NMR spectra were carried out by combined analyses of DEPT and ^1H−^{13}C correlated spectra (HSQC and HMBC). The assignment of the amido protons are based on combined analyses of the ^1H heteronuclear correlated spectra (^1H,^{15}N-HSQC and ^1H,^{29}Si-HMBC). The UV/vis spectra were recorded on a Cary 50 spectrometer in 1 cm quartz cuvettes. A Haake NK 22 refrigerated circulator bath was used for thermostating of the cuvettes. Elemental analyses were performed by Zentrale Elementaranalyse, Universität Hamburg. Deuterated solvents were purchased from euriso-top and dried over sodium benzophenone ketyl. Substituted triarylsilanes were purchased from Aldrich Chemical Co. (library of rare chemicals) and used as received, except for p-F_3C-$ArPh_2SiH$[42] and p-Me_2N-$ArPh_2SiH$[43] as well as (3-butenyl)dimethylsilane[18] and trimethylsilane,[44] which were prepared according to literature procedures. Spectroscopic data for these three silanes are given in the Supporting Information. All other reagents were purchased from the Aldrich Chemical Co., ABCR, Fluka, or Merck Chemicals and used as received. The nitrido complex [Ir(^{i}Pr$_4$N$_3$)N] (**1**) was prepared as described previously by us.[8,10]

Preparation of [Ir(^{i}Pr$_4$N$_3$)NHSiEt$_3$] (2). First, 2 mL (1.5 g, 3 mmol) of Et_3SiH was added to a violet stirred solution of **1** (96 mg, 0.14 mmol) in 8 mL of toluene. The solution was stirred for 4.5 h at room temperature, upon which the color changed to brown. The solvent was removed in vacuum, and the remaining volatiles were removed by co-evaporating with three portions of 5 mL of pentane. The crude product was recrystallized from a concentrated THF solution (∼1.5 mL) layered with HMDSO at −35 °C, yielding 49 mg (0.06 mmol, 43%) of complex **2** as a brown crystalline solid. A second crop could be obtained by analogous crystallization from the mother liquor, giving a combined yield of 64%. Single crystals suitable for X-ray diffraction were obtained by slow evaporation of a pentane solution containing a few drops of THF at −35 °C. ^1H NMR (400 MHz; THF-d_8) δ [ppm]: 8.47 (d, 2H, ^3J = 7.8 Hz; $C_{py}(3,5)\boldsymbol{H}$); 8.15 (t, 1H, ^3J = 7.8 Hz $C_{py}(4)\boldsymbol{H}$); 7.54 (s (br), 1H, N$\boldsymbol{H}$); 7.34 (m, 2H, $C_{arom}(4)\boldsymbol{H}$); 7.27 (m, 4H, $C_{arom}(3,5)\boldsymbol{H}$); 2.85 (sept, 4H, ^3J = 6.9 Hz, C$\boldsymbol{H}$(CH$_3$)$_2$); 1.08 (d, 12H, ^3J = 6.9 Hz, CH(C$\boldsymbol{H}_3$)$_2$); 0.96 (d, 12H, ^3J = 6.8 Hz, CH(C$\boldsymbol{H}_3$)$_2$); 0.83 (s, 6H, N═CC$\boldsymbol{H}_3$); 0.54 (t, 9H, ^3J = 8.0 Hz, Si-(CH$_2$C$\boldsymbol{H}_3$)$_3$); −0.05 (q, 6H, ^3J = 8.0 Hz, Si-(C$\boldsymbol{H}_2$CH$_3$)$_3$). ^1H NMR (400 MHz; THF-d_8; −55 °C) δ [ppm]: 8.57 (d, 2H; ^3J = 7.8 Hz; $C_{py}(3,5)\boldsymbol{H}$); 8.21 (t, 1H, ^3J = 7.8 Hz, $C_{py}(4)\boldsymbol{H}$); 7.45 (s (br), 1H, N$\boldsymbol{H}$); 7.42−7.25 (m (br), 6H, $C_{arom}(3,4,5)\boldsymbol{H}$); 2.79 (mc, 4H, C$\boldsymbol{H}$(CH$_3$)$_2$); 1.16−0.88 (m (br), 24H, CH(C$\boldsymbol{H}_3$)$_2$); 0.84 (s (br), 6H, N═CC$\boldsymbol{H}_3$); 0.51 (t, 9H, ^3J = 8.0 Hz, Si-(CH$_2$C$\boldsymbol{H}_3$)$_3$); −0.08 (q,

dx.doi.org/10.1021/ja311905h | J. Am. Chem. Soc. 2013, 135, 3971−3982

6H, ^3J = 8.0 Hz, Si-(CH_2CH$_3$)$_3$). ^{13}C{^{1}H} NMR (100 MHz; THF-d_8; −55 °C) δ [ppm]: 165 (N=CCH$_3$); 158 (C_{py}(2,6)); 147 (C_{arom}(1)); 142 (C_{arom}(2,6)); 128 and 124.8 (C_{arom}(3,4,5)); 123 (C_{py}(2,6)); 116.4 (C_{py}(4)); 28.4 (CH(CH$_3$)$_2$); 24.9 and 24.2 (CH(CH$_3$)$_2$); 21.5 (N=CCH$_3$); 9.2 (Si-(CH$_2$$CH_3$)$_3$); 9.0 (Si-($CH_2CH_3$)$_3$). ^{1}H,^{15}N-HSQC (400 MHz/41 MHz, THF-d_8, −55 °C) δ [ppm]: 130 (IrNH−Si(Et$_3$)). ^{1}H,^{29}Si-HMBC (400/79 MHz, THF-d_8, −55 °C) δ [ppm]: 15 (IrNH-Si(Et$_3$)). UV/vis (THF) λ_{max} [nm]: 439, 493, 549(sh), 585, 634(sh), 706. Elemental analysis calcd for $C_{39}H_{59}IrN_4Si$: C 58.25%, H 7.39%, N 6.97%, found C 57.76%, H 7.42%, N 6.82%.

Preparation of [Ir(^{i}Pr$_4$N$_3$)NHSiPh$_3$] (3-H). A solution of 109 mg (0.158 mmol) of **1** in 8 mL of toluene was added to a stirred solution of 821 mg (3.15 mmol) of Ph$_3$SiH in 5 mL of toluene. The solution was further stirred for 4.5 h at room temperature, upon which the solvent was removed in vacuum. Residual solvent was removed by co-evaporating the remaining brown oil with two portions of 5 mL of pentane. After 2 h of additional drying in vacuum, 2 mL of pentane was added to the brown oil, resulting in precipitation of the green product, which was collected by filtration and washed with 15 mL of pentane. The raw product was then recrystallized from a concentrated THF solution, layered with pentane at −35 °C. The supernatant was decanted, and the residual solid was washed with 10 mL of pentane. For the removal of co-crystallized solvents, the green crystals were dissolved four times in 5 mL of THF, dried in vacuum, and washed with 20 mL of pentane, yielding 82 mg (86.5 μmol; 55%) of a green solid. Single crystals suitable for X-ray diffraction were obtained from a THF solution layered with pentane at −35 °C. ^{1}H NMR (400 MHz; THF-d_8) δ [ppm]: 8.33 (m, 3H, C_{py}(3,4,5)H), 7.59 (s (br), 1H, NH), 7.09−6.85 (m, 21H, C_{arom}(3,4,5)H and Si-(C$_6H_5$)$_3$), 2.92 (sept, 4H, ^3J = 6.6 Hz, CH(CH$_3$)$_2$), 0.98 (d, 12H, ^3J = 6.8 Hz, CH(CH_3)$_2$), 0.83 (s 6H, N=CCH_3), 0.61 (d, 12H, ^3J = 6.7 Hz, CH(CH_3)$_2$). ^{13}C{^{1}H} NMR (100 MHz; THF-d_8) δ [ppm]: 167.8 (N=CCH$_3$); 159.4 (C_{py}(2,6)), 150.8, 142.3, 141.8 (C_{arom}(1,2,6) and Si-C(1)); 136.7, 128.7, 128.4, 127.7, 124.7 (C_{arom}(3,4,5) and Si-C(2,3,4,5,6)); 123.5, 117 (C_{py}(3,4,5)); 28.3 (CH(CH$_3$)$_2$); 24.6 (CH(CH$_3$)$_2$); 21.9 (N=CCH$_3$). ^{1}H,^{15}N-HSQC (400 MHz/41 MHz, THF-d_8) δ [ppm]: 97 (IrNH−Si(Ph$_3$)). ^{1}H,^{29}Si-HMBC (400/79 MHz, THF-d_8) δ [ppm]: −12 (IrNH-Si(Ph$_3$)). UV/vis (THF) λ_{max} [nm]: 436, 489, 553(sh), 590, 643, 708(sh). Elemental analysis calcd for $C_{51}H_{59}IrN_4Si$: C 64.59%, H 6.27%, N 5.9%, found C 64.18%, H 6.46%, N 5.66%.

Preparation of [Ir(^{i}Pr$_4$N$_3$)NHSiPh$_2$Ar-NMe$_2$] (3-NMe$_2$). A solution of 42 mg (0.061 mmol) of **1** in 5 mL of toluene was added to a stirred solution of 98 mg (0.32 mmol) p-Me$_2$N-ArPh$_2$SiH in 3 mL of toluene. The solution was stirred for 4.5 h at room temperature, and the solvent was then removed in vacuum. The oily residue was co-evaporated with 3 mL of pentane, suspended in 1 mL of pentane, and kept in a freezer at −35 °C overnight. The supernatant was then decanted from the solid residue, which was washed with six portions of cold (−35 °C) pentane (0.5 mL each), dried in vacuum, and co-evaporated with 3 mL of pentane. The raw product was then recrystallized from a pentane/THF solution (5:1), yielding 41 mg (0.041 mmol, 67%) of the green complex **3-NMe$_2$**, which was washed with four portions of cold (−35 °C) pentane (0.5 mL each) and dried in vacuum. ^{1}H NMR (500 MHz; THF-d_8) δ [ppm]: 8.35 (m, 2H, C_{py}(3,5)H); 8.27 (m, 1H, C_{py}(4)H); 7.81 (s (br), 1H, NH); 7.05−6.85 (m, 18H, C_{ar}(2,6)H, C_{ph}(2,3,4,5,6)H and C_{arom}(3,4,5)H); 6.39 (m, 2H, C_{ar}(3,5)H), 2.92 (sept, 4H, ^3J = 6.8 Hz, CH(CH$_3$)$_2$); 2.87 (s, 6H, N(CH_3)$_2$); 0.98 (d, 12H, ^3J = 6.9 Hz, CH(CH_3)$_2$); 0.83 (s, 6H, N=CCH_3); 0.63 (d, 12H, ^3J = 6.8 Hz, CH(CH_3)$_2$). ^{13}C{^{1}H} NMR (100 MHz; THF-d_8) δ [ppm]: 167.1 (N=CCH$_3$); 159.2 (C_{py}(2,6)); 151.5 (C_{ar}(4)); 150.9 (C_{arom}(1)); 143.4 (C_{ph}(1)); 141.8 (C_{arom}(2,6)); 137.8, 136.6, 128.6, 128.1, 127.5, 124.7 (C_{ar}(3,5), C_{ph}(2,3,4,5,6) and C_{arom}(3,4,5)); 127.4 (C_{ar}(1)); 123.3 (C_{py}(3,5)); 117.3 (C_{py}(4)); 112.5 (C_{ar}(3,5)); 40.6 (N(CH$_3$)$_2$); 28.3 (CH(CH$_3$)$_2$); 24.6 (CH(CH$_3$)$_2$); 22.0 (N=CCH$_3$). ^{1}H,^{15}N-HSQC (400 MHz/41 MHz, THF-d_8) δ [ppm]: 101 (IrNH−Si). ^{1}H,^{29}Si-HMBC (400/79 MHz, THF-d_8) δ [ppm]: −13 (IrNH-Si).

Preparation of [Ir(^{i}Pr$_4$N$_3$)NHSiPh$_2$Ar−CF$_3$] (3-CF$_3$). A solution of 45 mg (0.065 mmol) of **1** in 5 mL of toluene was added to a stirred solution of 114 mg (0.347 mmol) of p-F$_3$C-ArPh$_2$SiH in 3 mL of toluene. The solution was stirred for 2.5 h at room temperature, and the solvent was then removed in vacuum. The oily residue was co-evaporated with 3 mL of pentane, suspended in 2 mL of pentane, and kept overnight in a freezer at −35 °C. The suspension was filtered, and the obtained solid residue was washed with three portions of cold (−35 °C) pentane (0.5 mL each) and finally dried in vacuum. The raw product was then recrystallized twice at −35 °C from a THF solution layered with pentane. The crystalline product was washed with 5−6 portions of cold (−35 °C) pentane (0.5−1 mL) and dried in vacuum, yielding 22 mg (0.022 mmol, 34%) of complex **3-CF$_3$**. Single crystals suitable for X-ray diffraction were obtained at −35 °C from a pentane solution containing a few drops of THF. ^{1}H NMR (500 MHz; THF-d_8) δ [ppm]: 8.37 (m, 1H, $C_{py}$$H$(3,5)); 7.31 (s (br), 1H, NH); 7.25 (m, 2H, $C_{ar}$$H$(3,5)); 7.20 (m, 2H, $C_{ar}$$H$(2,6)); 7.08 (m, 2H $C_{ph}$$H$(4)); 7.04−6.95 (m, 10H, $C_{ph}$$H$(2,3,5,6) and $C_{arom}$$H$(4)); 6.91 (m, 4H, $C_{arom}$$H$(3,5)); 2.92 (sept, 4H, ^3J = 6.8 Hz, CH(CH$_3$)$_2$); 0.99 (d, 12H, ^3J = 6.8 Hz, CH(CH_3)$_2$); 0.85 (s, 6H, N=CCH_3); 0.62 (d, 12H, ^3J = 6.8 Hz, CH(CH$_3$)$_2$). ^{13}C{^{1}H} NMR (100 MHz; THF-d_8) δ [ppm]: 168.5 (N=CCH$_3$); 159.5 (C_{py}(2,6)); 150.8 (C_{arom}(1)); 148.2 (C_{ar}(1)); 141.8 (C_{arom}(2,6)); 141.3 (C_{ph}(1)); 136.9 (C_{ar}(2,6)); 127.9, 128.7, 136.7 (C_{ph}(2,3,5,6) and C_{arom}(4)); 128.9 (C_{ph}(4)); 124.7 (C_{arom}(3,5)); 124.2 (q, $^3J_{F,C}$ = 4 Hz, C_{ar}(3,5)); 123.8 (C_{py}(3,5)); 118.0 (C_{py}(4)); 28.3 (CH(CH$_3$)$_2$); 24.57, 24.59 (CH(CH$_3$)$_2$); 22.0 (N=CCH$_3$). The quartets for the CF$_3$ and C_{ar}(4) carbon atoms could not be detected. ^{1}H,^{15}N-HSQC (400 MHz/41 MHz, THF-d_8) δ [ppm]: 87 (IrNH−Si). ^{19}F NMR δ [ppm] = −61.7 (CF_3). ^{1}H,^{29}Si-HMBC (400/79 MHz, THF-d_8) δ [ppm]: −14 (IrNH-Si).

Preparation of [Ir(^{i}Pr$_4$N$_3$)NHSiMe$_2$-3-butene] (4). A solution of 77 mg (0.67 mmol) of (3-butenyl)dimethylsilane in 2 mL of toluene was added to a stirred solution of 99 mg (0.14 mmol) of **1** in 8 mL of toluene. The reaction solution was stirred at room temperature for 1 h. The solvent and excess silane was removed in vacuum, and the remaining volatiles were removed by co-evaporating with 3 mL of pentane. The crude product was recrystallized from a concentrated THF/HMDSO (1:10) solution at −35 °C to yield 71 mg (0.089 mmol; 64%) of the brown complex **4**, which was washed with three portions of 1 mL of cold (−35 °C) HMDSO. A second crop could be obtained by analogous crystallization from the mother liquor, giving a combined yield of 82%. Alternatively, complex **4** can be recrystallized from a concentrated toluene solution at −35 °C with comparable yield. In repeated attempts, correct elemental analysis data were obtained for one batch only (vide infra). All other measurements gave too-high carbon values. Single crystals suitable for X-ray diffraction were obtained by slow evaporation of a pentane solution containing a few drops of THF at −35 °C. ^{1}H NMR (400 MHz; C$_6$D$_6$) δ [ppm]: 7.97 (m, 2H, C_{py}(3,5)H); 7.89 (s (br), 1H, NH); 7.83 (m, 1H, C_{py}(4)H); 7.30 (m, 2H, C_{arom}(4)H); 7.22 (m, 4H, C_{arom}(3,5)H); 5.99 (ddt, 1H, $^3J_{cis}$ = 16.9 Hz, $^3J_{trans}$ = 10.2 Hz, ^3J = 6.2 Hz, Si-CH$_2$−CH$_2$−CH=CH$_2$); 5.11 (ddt, 1H, ^2J = 2.2 Hz, ^3J = 16.9 Hz, ^4J = 1.7 Hz, Si-CH$_2$−CH$_2$−CH=CH_2), 5.02 (ddt, 1H, ^2J = 2.2 Hz, ^3J = 10.2 Hz, ^4J = 1.4 Hz, Si-CH$_2$−CH$_2$−CH=CH_2); 2.99 (sept, 4H, ^3J = 6.9 Hz, CH(CH$_3$)$_2$); 1.98−1.91 (m, 2H, Si-CH$_2$−CH_2-CH=CH$_2$); 1.16 (d, 12H, ^3J = 6.8 Hz, CH(CH_3)$_2$); 0.99 (d, 12H, ^3J = 6.9 Hz, CH(CH_3)$_2$); 0.51 (s, 6 Hz, N=CCH_3); 0.49−0.45 (m, 2H, Si−CH_2-CH$_2$−CH=CH$_2$); −0.13 (s, 6H, Si(CH_3)$_2$). ^{1}H NMR (400 MHz; THF-d_8) δ [ppm]: 8.48 (d, 2H, ^3J = 7.8 Hz, C_{py}(3,5)H); 8.16 (t, 1H, ^3J = 7.8 Hz, C_{py}(4)H); 7.38 (s (br), 1H, NH); 7.33 (m, 2H, C_{arom}(4)H); 7.27 (m, 4H, C_{arom}(3,5)H); 5.86 (ddt, 1H, $^3J_{cis}$ = 17.0 Hz, $^3J_{trans}$ = 10.1 Hz, ^3J = 6.2 Hz, Si-CH$_2$−CH$_2$−CH=CH$_2$); 4.79 (ddt, 1H, ^2J = 2.2 Hz, ^3J = 17.0 Hz, ^4J = 1.7 Hz, Si-CH$_2$−CH$_2$−CH=CH_2), 4.71 (ddt, 1H, ^2J = 2.2 Hz, ^3J = 10.1 Hz, ^4J = 1.4 Hz, Si-CH$_2$−CH$_2$−CH=CH_2); 2.84 (sept, 4H, ^3J = 6.8 Hz, CH(CH$_3$)$_2$); 1.64−1.56 (m, 2H, Si-CH$_2$−CH_2-CH=CH$_2$); 1.09 (d, 12H, ^3J = 7.0 Hz, CH(CH_3)$_2$); 0.94 (d, 12H, ^3J = 6.8 Hz, CH(CH_3)$_2$); 0.82 (s, 6 Hz, N=CCH_3); 0.10−0.04 (m, 2H, Si−CH_2-CH$_2$−CH=CH$_2$); −0.57 (s, 6H, Si(CH_3)$_2$). ^{13}C{^{1}H} NMR (100 MHz; THF-d_8) δ [ppm]: 164.4 (N=CCH$_3$); 158.1 (C_{py}(2,6)); 152 (C_{arom}(1)); 143.7 (Si-CH$_2$−CH$_2$-CH=CH$_2$); 142.3 (C_{arom}(2,6))); 128.0 (C_{arom}(4)); 124.5 (C_{arom}(3,5)); 122.6 (C_{py}(3,5)); 116.3 (C_{py}(4)); 112.0 (Si-CH$_2$−CH$_2$−CH=CH$_2$); 29.8 (Si-CH$_2$-CH$_2$−CH=CH$_2$); 28.5 (CH(CH$_3$)$_2$); 25.0 (CH(CH$_3$)$_2$);

dx.doi.org/10.1021/ja311905h | J. Am. Chem. Soc. 2013, 135, 3971−3982

24.1 ($CH(CH_3)_2$); 21.8 (Si-CH_2−CH_2−CH=CH_2); 21.1 (N=CCH_3); 3.2 (Si(CH_3)$_2$). ^{1}H,^{15}N-HSQC (400 MHz/41 MHz, THF-d_8) δ [ppm]: 136 (Ir**N**H−Si(Me)$_2$-CH_2−CH_2−CH=CH_2). ^{1}H,^{29}Si-HMBC (400/79 MHz, THF-d_8) δ [ppm]: 7 (IrNH-***Si***(Me)$_2$-CH_2−CH_2−CH=CH_2). Elemental analysis calcd for $C_{39}H_{57}IrN_4Si$: C 58.39%, H 7.16%, N 6.98%, found C 58.16%, H 7.20%, N 6.8%.

Reaction of Complex 1 with Et_3SiH Monitored by ^{1}H NMR Spectroscopy. First, 20 mg (33 μmol) of **1** and 15 mg (81 μmol) of ferrocene as internal standard were dissolved in 1 mL of THF-d_8. The solution was transferred to a NMR tube fitted to a Cajoin ultravacuum adapter attached to a J. Young high-vacuum tap. The NMR tube was then transferred to a high-vacuum manifold, and the solution was frozen in liquid nitrogen. A solution of 150 μL (109 mg; 0.937 mmol) of Et_3SiH in 0.5 mL of THF-d_8 was then added to the frozen complex solution using a gastight syringe. This mixture was frozen in liquid nitrogen, and the NMR tube was flame-sealed under a vacuum. The solutions were mixed by shaking the NMR tube at −50 °C in an acetone/N_2 bath. The NMR tube was then transferred to the pre-tempered NMR probe. After warming to 0 °C, the reaction was monitored by ^{1}H NMR spectroscopy at 0 °C every 6.5 min. Pseudo-first-order analysis of the kinetic data gave a rate constant k_{sec} = 3.8(2) ×10^{-3} L/mol·s at 0 °C.

General Procedure for the Determination of the Rate Constants. *Reaction of Complex 1 with Et_3SiH.*

(a) Slow to medium reaction rates (k_{obs} < 3 × 10^{-3} s^{-1}) and temperature-dependent measurements. In a glovebox, 4 mL of a stock solution of complex **1** (typically ∼0.8−1.0 μmol) was treated with a known amount of the silane with an Eppendorf pipet. The reaction solution was transferred to a 1 cm UV/vis cuvette fitted with a J. Young Teflon tap. The reaction progress was then monitored by the decay or increase of unique absorption bands (cf. Supporting Information.).

(b) Faster reaction rates (k_{obs} > 3 × 10^{-3} s^{-1}). First, 3 mL of a stock solution of complex **1** (typically ∼0.8−1.0 μmol) was transferred to a 1 cm UV/vis cuvette fitted with a septum seal in the glovebox and placed into the pre-tempered cuvette holder. The silane dissolved in 1 mL of the solvent was then added to the solution of the nitrido complex with a gastight syringe.

*Reaction of **1** with p-X-ArPh$_2$SiH.* In a nitrogen-filled glovebox, 2 mL (resp. 1 mL) of a stock solution of the silane was added to 2 mL (resp. 3 mL) of a stock solution of **1** (∼0.8 μmol) in THF. The reaction solution was transferred to a 1 cm UV/vis cuvette fitted with a J. Young Teflon tap. The reaction was then monitored in the pre-tempered instrument.

Computational Studies. *General Considerations and Methods.* The DFT calculations were carried out with the parallelized versions (rel. 6.2 and 6.3) of Turbomole[45,46] on our 192 and 272 core Intel Xeon (Harpertown & Nehalem) clusters. Unless otherwise specified, the geometries of the ground and transition states were optimized without symmetry restrictions (C_1-symmetry) until gradients smaller than 10^{-4} hartree/bohr were reached. The starting geometries and transition states were characterized as stationary points by the calculation of analytical second derivatives through the absence (ground states) or presence of one imaginary frequency (transition states). The transition states were further analyzed by IRC calculations, which assured the correct reaction paths. For the latter, the Gaussian 03 geometry optimizer[47] was used in combination with a perl script (Gau_external written by Karin Wichmann) interfacing to Turbomole.

We have probed for the contribution of possible triplet spin states (S = 1) in unrestricted calculations and found no reaction barriers lower than for the closed shell S = 0 states. The Becke−Perdew (BP-86) functional[48,49] was used for the geometry optimizations employing the resolution of identity (RI) methodology[50] available in Turbomole (ridft, rdgrad). The modified grids m4 and m5 of the Turbomole program were employed for the DFT calculations. For the iridium and silicon centers def2-TZVPP basis sets were applied. For the nitrogen atom of the nitrido ligand as well as the silane bonded hydrogen atom def2-TZVPP basis sets were employed, which were augmented by diffuse basis functions taken from the aug-cc-pVTZ basis sets of these atoms. Unless otherwise specified the def2-SVP basis sets were used for the residual atoms (C, H, Cl, N, O). For the iridium central atom, a Stuttgart (ECP-60-MWB) pseudopotential[51] was used throughout in the calculations. Analytical second derivatives were obtained for this set of basis functions unless otherwise specified. For some of the systems, both larger and smaller basis sets were employed, which are denoted accordingly in the Supporting Information along with their optimized coordinates.

The dependence of the energetics (thermodynamics and barriers) on the DFT functionals was probed for the reaction of the model system **1-model** + SiH_4 → [N_3Ir]N(SiH_3)(H) and was found to be negligible (all within 3 kcal/mol deviation). The PBE0,[52] B3LYP[53] hybrid functional, BP86,[48,49] PBE,[52] GGA functionals, and TPSS[54] meta-GGA and B2PLYP double hybrid functionals[55] were considered (cf. Supporting Information).

Furthermore, the basis set dependence for the reaction energetics of the model system **1-model** + SiH_4 → [N_3Ir]N(SiH_3)(H) was probed employing larger triple-ζ basis sets with polarization (def2-TZVPP) for all atoms. The derived values for the larger basis sets displayed only negligible deviations (all within 3 kcal/mol) from the results obtained for the smaller basis sets thus justifying our approach. Details are described in the Supporting Information.

NBO: Second-Order Perturbation Theory for TS_a. The utilized converged wave function was derived from a ZORA relativistic DFT calculation (BP-86 functional) with the ORCA 2.6.72 program[56,57] for the transition-state geometry of $\mathbf{TS_a}$ of the transformation **1** + $HSiPh_3$ → **3-H**. For the Ir center and residual atoms, all-electron basis sets (SVP) integrated in the Orca program package were employed. The second-order perturbation NBO analysis was performed with the NBO 5.0 program.[58] The figures were prepared by a combination of the Chemcraft[59] and VMD program suites.[60]

ALMO-EDA/CTA Calculations. ALMO-EDA/CTA calculations were performed with the Q-CHEM program package (rel. 3.2 and 4.0).[61] For the Ir center an LANL2DZ basis sets with the corresponding Los Alamos pseudopotential was employed, whereas for the residual atoms 6-31G** basis sets were utilized, augmented by a diffuse s-function for the nitrido nitrogen atom (6-31G**$^+$ basis). Larger basis sets did not give significantly different results. COVPs plots were prepared from cube files with the Vesta-3 program package.[62]

■ ASSOCIATED CONTENT

Ⓢ Supporting Information

Description of the syntheses, X-ray crystal structures, kinetic measurements, and analyses; further details of the DFT calculations; and geometry-optimized structures. This material is available free of charge via the Internet at http://pubs.acs.org.

■ AUTHOR INFORMATION

Corresponding Author

burger@chemie.uni-hamburg.de

Notes

The authors declare no competing financial interest.

■ ACKNOWLEDGMENTS

This paper is in honor of Prof. Hans-Herbert Brintzinger. We thank Ulrich Behrens for assistance with the crystal structure refinement. We are thankful to Bastian Wolff and Matthias Schreyer for their help with some of the experiments. Funding by Deutsche Forschungsgemeinschaft is gratefully acknowledged.

■ REFERENCES

(1) Walstrom, A.; Pink, M.; Yang, X.; Tomaszewski, J.; Baik, M.-H.; Caulton, K. G. *J. Am. Chem. Soc.* **2005**, *127*, 5330.

(2) Scepaniak, J. J.; Fulton, M. D.; Bontchev, R. P.; Duesler, E. N.; Kirk, M. L.; Smith, J. M. *J. Am. Chem. Soc.* **2008**, *130*, 10515.

(3) Pap, J. S.; DeBeer George, S.; Berry, J. F. *Angew. Chem., Int. Ed.* **2008**, *47*, 10102.
(4) Vogel, C.; Heinemann, F. W.; Sutter, J.; Anthon, C.; Meyer, K. *Angew. Chem., Int. Ed.* **2008**, *47*, 2681.
(5) Berry, J. F. *Comments Inorg. Chem.* **2009**, *30*, 28.
(6) Askevold, B.; Nieto, J. T.; Tussupbayev, S.; Diefenbach, M.; Herdtweck, E.; Holthausen, M. C.; Schneider, S. *Nature Chem.* **2011**, *3*, 532.
(7) Scheibel, M. G.; Askevold, B.; Heinemann, F. W.; Reijerse, E. J.; deBruin, B.; Schneider, S. *Nature Chem.* **2012**, *4*, 552.
(8) Schöffel, J.; Rogachev, A. Y.; DeBeer George, S.; Burger, P. *Angew. Chem., Int. Ed.* **2009**, *48*, 4734.
(9) Betley, T. A.; Peters, J. C. *J. Am. Chem. Soc.* **2004**, *126*, 6252.
(10) Schöffel, J.; Šušnjar, N.; Nückel, S.; Sieh, D.; Burger, P. *Eur. J. Inorg. Chem.* **2010**, 4911.
(11) Long, A. K. M.; Timmer, G. H.; Pap, J. S.; Snyder, J. L.; Yu, R. P.; Berry, J. F. *J. Am. Chem. Soc.* **2011**, *133*, 13138.
(12) Long, A. K. M.; Yu, R. P.; Timmer, G. H.; Berry, J. F. *J. Am. Chem. Soc.* **2010**, *132*, 12228.
(13) Hojilla Atienza, C. C.; Bowman, A. C.; Lobkovsky, E.; Chirik, P. J. *J. Am. Chem. Soc.* **2010**, *132*, 16343.
(14) Sieh, D.; Schöffel, J.; Burger, P. *Dalton Trans.* **2011**, *40*, 9512.
(15) Scepaniak, J. J.; Young, J. A.; Bontchev, R. P.; Smith, J. M. *Angew. Chem., Int. Ed.* **2009**, *48*, 3158.
(16) Schlangen, M.; Neugebauer, J.; Reiher, M.; Schröder, D.; López, J. P.; Haryono, M.; Heinemann, F. W.; Grohmann, A.; Schwarz, H. *J. Am. Chem. Soc.* **2008**, *130*, 4285.
(17) Eyring, H. *J. Chem. Phys.* **1935**, *3*, 107.
(18) Barton, T. J.; Revis, A. *J. Am. Chem. Soc.* **1984**, *106*, 3802.
(19) Chatgilialoglu, C. *Organosilanes in Radical Chemistry*; John Wiley & Sons, Ltd.: Chichester: 2004.
(20) Chatgilialoglu, C.; Woynar, H.; Ingold, K. U.; Davies, A. G. *J. Chem. Soc., Perkin Trans. 2* **1983**, 555.
(21) Hansch, C.; Leo, A.; Taft, R. W. *Chem. Rev.* **1991**, *91*, 165.
(22) Brown, H. C.; Okamoto, Y. *J. Am. Chem. Soc.* **1958**, *80*, 4979.
(23) *Advances in Linear Free Energy Relationships*; Chapman, N. B., Shorter, J., Eds.; Plenum Press: New York, 1972.
(24) The animated IRC paths of the model system are included in the Supporting Information as Shockwave (.swf) files, which can be viewed in a Web browser.
(25) Badenhoop, J. K.; Weinhold, F. *J. Chem. Phys.* **1997**, *107*, 5406.
(26) Badenhoop, J. K.; Weinhold, F. *J. Chem. Phys.* **1997**, *107*, 5422.
(27) Weinhold, F.; Landis, C. R. *Discovering Chemistry with Natural Bond Orbitals*; John Wiley & Sons: Hoboken, NJ, 2012.
(28) Khaliullin, R. Z.; Bell, A. T.; Head-Gordon, M. *J. Chem. Phys.* **2008**, *128*, 184112.
(29) Khaliullin, R. Z.; Cobar, E. A.; Lochan, R. C.; Bell, A. T.; Head-Gordon, M. *J. Phys. Chem. A* **2007**, *111*, 8753.
(30) Ess, D. H.; Bischof, S. M.; Oxgaard, J.; Periana, R. A.; Goddard, W. A. *Organometallics* **2008**, *27*, 6440.
(31) Ess, D. H.; Goddard, W. A.; Periana, R. A. *Organometallics* **2010**, *29*, 6459.
(32) Gorelsky, S. I. *J. Chem. Theory Comput.* **2012**, *8*, 908.
(33) Gorelsky, S. I. *AOMIX 6.6*, 2012; http://www.sg-chem.net/.
(34) Huber, K. P.; Herzberg, G. Constants of Diatomic Molecules. *Molecular Spectra and Molecular Structure. IV*; Van Nostrand: New York, 1979.
(35) Hirota, E. *J. Mol. Spectrosc.* **1979**, *77*, 213.
(36) Timmer, G. H.; Berry, J. F. *Chem. Sci.* **2012**, *3*, 3038.
(37) Hedegård, E. D.; Bendix, J.; Sauer, S. P. A. *J. Mol. Struct. (Theochem)* **2009**, *913*, 1.
(38) Costas, M. *Coord. Chem. Rev.* **2011**, *255*, 2912.
(39) Newcomb, M.; Shen, R.; Choi, S.-Y.; Toy, P. H.; Hollenberg, P. F.; Vaz, A. D. N.; Coon, M. J. *J. Am. Chem. Soc.* **2000**, *122*, 2677.
(40) Shaik, S.; de Visser, S. P.; Ogliaro, F.; Schwarz, H.; Schröder, D. *Curr. Opin. Chem. Biol.* **2002**, *6*, 556.
(41) Ogliaro, F.; Harris, N.; Cohen, S.; Filatov, M.; de Visser, S. P.; Shaik, S. *J. Am. Chem. Soc.* **2000**, *122*, 8977.
(42) Allen, J. M.; Aprahamian, S. L.; Sans, E. A.; Shechter, H. *J. Org. Chem.* **2002**, *67*, 3561.
(43) Gilman, H.; Dunn, G. E. *J. Am. Chem. Soc.* **1951**, *73*, 3404.
(44) Steward, O. W.; Pierce, O. R. *J. Am. Chem. Soc.* **1961**, *83*, 1916.
(45) Ahlrichs, R.; Bär, M.; Häser, M.; Horn, H.; Kölmel, C. *Chem. Phys. Lett.* **1989**, *162*, 165.
(46) *TURBOMOLE*, V6.2 and 6.3; University of Karlsruhe and Forschungszentrum Karlsruhe GmbH, 1989−2007; TURBOMOLE GmbH, since 2007; 2010−11; http://www.turbomole.com.
(47) Frisch, M. J.; Trucks, G. W.; Schlegel, H. B.; Scuseria, G. E.; Robb, M. A.; Cheeseman, J. R., Montgomery, J. A., Jr.; Vreven, T.; Kudin, K. N.; Burant, J. C.; Millam, J. M.; Iyengar, S. S.; Tomasi, J.; Barone, V.; Mennucci, B.; Cossi, M.; Scalmani, G.; Rega, G. A.; Petersson, N.; Nakatsuji, H.; Hada, M.; Ehara, M.; Toyota, K.; Fukuda, R.; Hasegawa, J.; Ishida, M.; Nakajima, T.; Honda, Y.; Kitao, O.; Nakai, H.; Klene, M.; Li, X.; Knox, J. E.; Hratchian, H. P.; Cross, J. B.; Bakken, V.; Adamo, C.; Jaramillo, J.; Gomperts, R.; Stratmann, R. E.; Yazyev, O.; Austin, A. J.; Cammi, R.; Pomelli, C.; Ochterski, J. W.; Ayala, P. Y.; Morokuma, K.; Voth, G. A.; Salvador, P.; Dannenberg, J. J.; Zakrzewski, V. G.; Dapprich, S.; Daniels, A. D.; Strain, M. C.; Farkas, O.; Malick, D. K.; Rabuck, A. D.; Raghavachari, K.; Foresman, J. B.; Ortiz, J. V.; Cui, Q.; Baboul, A. G.; Clifford, S.; Cioslowski, J.; Stefanov, B. B.; Liu, G.; Liashenko, A.; Piskorz, P.; Komaromi, I.; Martin, R. L.; Fox, D. J.; Keith, T.; Al-Laham, M. A.; Peng, C. Y.; Nanayakkara, A.; Challacombe, M.; Gill, P. M. W.; Johnson, B.; Chen, W.; Wong, M. W.; Gonzalez, C.; Pople, J. A. *Gaussian 03*; Gaussian, Inc.: Wallingford, CT, 2004.
(48) Becke, A. D. *Phys. Rev. A* **1988**, *38*, 3098.
(49) Perdew, J. P. *Phys. Rev. B* **1986**, *33*, 8822.
(50) Treutler, O.; Ahlrichs, R. *J. Chem. Phys.* **1995**, *102*, 346.
(51) Andrae, D.; Haeussermann, U.; Dolg, M.; Stoll, H.; Preuss, H. *Theor. Chim. Acta.* **1990**, *77*, 1431.
(52) Perdew, J. P.; Burke, K.; Ernzerhof, M. *Phys. Rev. Lett.* **1996**, *77*, 3865.
(53) Becke, A. D. *J. Chem. Phys.* **1993**, *98*, 5648.
(54) Tao, J.; Perdew, J. P.; Staroverov, V. N.; Scuseria, G. E. *Phys. Rev. Lett.* **2003**, *91*, 146401.
(55) Grimme, S. *J. Chem. Phys.* **2006**, *124*, 034108.
(56) Bühl, M.; Reimann, C.; Pantazis, D. A.; Bredow, T.; Neese, F. *J. Chem. Theor. Comput.* **2009**, *5*, 2220.
(57) Pantazis, D. A.; Chen, X.-Y.; Landis, C. R.; Neese, F. *J. Chem. Theor. Comput.* **2008**, *4*, 908.
(58) Reed, A. E.; Weinstock, R. B.; Weinhold, F. *J. Chem. Phys.* **1985**, *83*, 735.
(59) http://www.chemcraftprog.com.
(60) Humphrey, W.; Dalke, A.; Schulten, K. *J. Mol. Graphics* **1996**, *14*, 33.
(61) Shao, Y.; Fusti-Molnar, L.; Jung, Y.; Kussmann, J.; Ochsenfeld, C.; Brown, S. T.; Gilbert, A. T. B.; Slipchenko, L. V.; Levchenko, S. V.; O'Neill, D. P.; DiStasio, R. A., Jr.; Lochan, R. C.; Wang, T.; Beran, G. J. O.; Besley, N. A.; Herbert, J. M.; Lin, C. Y.; Van Voorhis, T.; Chien, S. H.; Sodt, A.; Steele, R. P.; Rassolov, V. A.; Maslen, P. E.; Korambath, P. P.; Adamson, R. D.; Austin, B.; Baker, J.; Byrd, E. F. C.; Daschel, H.; Doerksen, R. J.; Dreuw, A.; Dunietz, B. D.; Dutoi, A. D.; Furlani, T. R.; Gwaltney, S. R.; Heyden, A.; Hirata, S.; Hsu, C.-P.; Kedziora, G.; Khaliullin, R. Z.; Klunzinger, P.; A.M., L.; Lee, M. S.; Liang, W.; Lotan, I.; Nair, N.; Peters, B.; Proynov, E. I.; Pieniazek, P. A.; Rhee, Y. M.; Ritchie, J.; Rosta, E.; Sherrill, C. D.; Simmonett, A. C.; Subotnik, J. E.; Woodcock, H. L., III; Zhang, W.; Bell, A. T.; Chakraborty, A. K.; Chipman, D. M.; Keil, F. J.; Warshel, A.; Hehre, W. J.; Schaefer, H. F., III; Kong, J.; Krylov, A. I.; Gill, P. M. W.; Head-Gordon, M. *Phys. Chem. Chem. Phys.* **2006**, *8*, 3172.
(62) Momma, K.; Izumi, F. *J. Appl. Crystallogr.* **2011**, *44*, 1272.